Supplemental information

Bi-molecular Kinetic Competition for Surface Passivation in High-Performance Perovskite Solar Cells

Yinyi Ma[1], Faming Li[1], Jue Gong[1], Lina Wang[1], Xiao Tang[1], Peng Zeng[1], Pok Fung Chan[3], Weidong Zhu[4], Chunfu Zhang[4], and Mingzhen Liu[1, 2,]*

1 School of Materials and Energy, University of Electronic Science and Technology of China, Chengdu 611731, P.R. China.

2 State Key Laboratory Electronic Thin Film and Integrated Devices, University of Electronic Science and Technology of China, Chengdu 611731, P.R. China.

3 Department of Physics. The Chinese University of Hong Kong Shatin, Hong Kong SAR 999077, China

4 State Key Discipline Laboratory of Wide Band Gap Semiconductor Technology and Shaanxi Joint Key Laboratory of Graphene, School of Microelectronics, Xidian University, Xi'an, 710071, P.R. China.

*Correspondence: E-mail: mingzhen.liu@uestc.edu.cn (M.Z.L.)

Methods

***Materials*:** Materials used in experiments include FAI (99.9%, Dyesol), MAI (99.9%, Dyesol), lithium bis(trifluoromethanesulfonyl)imide (Li-TFSI, 99.95%, Sigma-Aldrich), SnO_2 colloid precursor (Alfa Aesar, tin(IV) oxide, 15% in H_2O colloidal dispersion), 4-tertbutylpyridine (4-tBP, 96%, Sigma-Aldrich), chlorobenzene (Sigma-Aldrich), N,N-dimethyiformamide (DMF, 99.8%, Sigma-Aldrich), dimethylsulfoxide (DMSO, 99.5%, Sigma-Aldrich), isopropanol (99.99%, Sigma-Aldrich), PbI_2 (99.99%, Sigma-Aldrich), Spiro-OMeTAD (99.8%, Borun New Material Technology), MACl (99.9%), OAI (99.9%) and PMAI (99.5%) were purchased from Xi'an Polymer Light Technology in China. All chemicals were directly used without any further purification.

***Device fabrication*:** Fluorine-tin-oxide (FTO) glass was cleaned by ultrasonic cleaner using acetone and ethanol sequentially. Before use, the FTO was cleaned with ultraviolet ozone for 30 min. Then SnO_2 colloid solution diluted by water (1:5) was spin coated on the substrate at 3000 rpm for 30 s, and annealed in ambient air at 150 ℃ for 30 min. It is better to clean the substrate with ultraviolet ozone for 10 min before preparation of perovskite films. First, 1.5 M of PbI_2 in DMF: DMSO (9:1) solvent stirred at 70 ℃ overnight was spin-coated on the SnO_2 substrate at 1500 rpm for 30 s, then annealed at 70 ℃ for 1 min. After cooling down, the FAI/MAI/MACl (90 mg: 6 mg: 9 mg in 1 ml IPA) solution was subsequently spin-coated on the PbI_2 layer at 2000 rpm for 30 s. Then, the film was annealed at 150 ℃ for 15 min in air (30-40% humidity). After perovskite formation, the samples were transferred to glove box for further processing. For a single passivation treatment, the PMAI and OAI were dissolved separately in IPA solution and spin-coated on the perovskite surface at 5000 rpm for 30 s. For bi-molecular passivation treatment. PMAI (35 mM) and OAI (10 mM) were dissolved in the same bottle of IPA solution and spin-coated on the perovskite surface at 5500 rpm for 30 s. Finally, the hole-transport layer was deposited by spin-coating the Spiro-OMeTAD solution at 3000 rpm for 30 s on the top of perovskite film, which consisted of 73.4 mg Spiro-OMeTAD, 17.6 μL Li-TFSI solution (520 mg Li-TFSI in 1 mL ACN) and 28.8 μL 4-tBP in 1 mL CB. At last, 100 nm Au electrode was thermally

evaporated on top of the Spiro-OMeTAD layer.

Optimized high-efficiency device fabrication conditions: Except for slightly changing the preparation method of the perovskite layer, the preparation method of the rest of the layers is the same as above. Specifically, 1.55 M PbI_2 were dissolved in DMF/DMSO (95:5) solvent, the rotation speed was adjusted to 1300 rpm for 30 s, and then preheated on a 70 ℃ for 10 s. The organic salt solution FAI/MAI/MACl (95 mg: 7 mg: 10 mg in 1 ml IPA) were quickly dropped on the PbI_2 films and spin-coated at 1800rpm for 30 s. In addition, in order to increase the optical transmittance of the device surface, a 120 nm LiF anti-reflection layer was thermally deposited on the back of the glass substrate.

Device Characterizations: Bruker D8 Advance diffractometer with Cu Kα radiation (λ = 1.5418 Å) and LYNXEYE_XE detector was used to record X-ray diffraction patterns of films and powders. Grazing incidence wide-angle X-ray scattering (GIWAXS) measurements were conducted at a Xeuss 2.0 SAXS/WAXS laboratory beamline equipped with a Cu X-ray source (8.05 keV, 1.54 Å) and a Pilatus3R 300K detector. Three incident angles (0.1° and 0.5°) were selected to represent the crystal structure of perovskite with different depths. Scanning electron microscope images were gained by FEI Inspect F50 electron microscope with electron energy of 10 keV. Steady-state and time-resolved PL decays were characterized by using FluoTime300 (PicoQuant). For PL measurements, the background subtractions were performed by multi-exponential fittings with a constant term. For the temperature-dependent PL measurement, we tested PL curves every 10 K from 70 K to 300 K, the samples were placed in a helium compressor system (Advanced Research Systems). X-ray photoelectron spectroscopy (XPS) was detected by the Thermo Fisher Scientific Escalab 250Xi system by using a He discharge lamp (21.22 eV). The XPS spectra were calibrated using inorganic carbon at 284.8 eV. The J-V curves were measured by Keithley 2400 digital source-meter and the devices were placed under simulated AM 1.5G irradiation (100 mW/cm^2, xenon lamp, Newport). The effective area of the cell was defined by a metal mask (device area: 0.09 cm^2; measurement mask size: 0.0491 cm^2). The electrochemical impedance spectra (EIS) of the solar cells were obtained by an electrochemical workstation (ZAHNER). Mott–Schottky analysis of the data was measured at a frequency of 1 kHz

with bias potentials from 0 to 1 V. The KPFM measurements were conducted by an AFM (KEYSIGHT Technologies 7500) with a Pt-coated conductive cantilever probe (Bruker, Model: SCM-PIT-V2). Transient photocurrent (TPC) measurement was performed with a system excited by a 532 nm (1000 Hz, 3.2 ns) pulse laser. Transient photo voltage (TPV) measurement was performed with the same system excited by a 405 nm CW laser (MDL-III-405). A digital oscilloscope (Tektronix, MSO5204B) was used to record the photocurrent or photovoltage decay process with a sampling resistor of 50 Ω or 1 MΩ, respectively. EQE spectra are performed through Enli Technology QE-R.

Stability Tests: The devices used for stability testing are all uncapsulation. To ensure the stability of the ambient humidity, the devices were placed under dark ambient conditions (RH: 30±5%, temperature: 25°C). Operation stability measurement were performed MPP tracking under continuous illumination from a full AM1.5 sun-equivalent white LED lamp in N_2 atmosphere, followed by normalizing the PCEs measured before aging.

Density Functional Theory Calculation: We use first-principles excited states molecular dynamics methods with CP2K/Quickstep[1] to study the adsorption, formation processes of OA, PMA and perovskite. Molecular dynamics algorithm combined with NVT ensemble, Nose-Hover thermostat[2, 3], 0.1 fs step size, 30,000 steps. The force and velocity are calculated using density functional theory (DFT)[4] for BLYP functional[5], Gaussian-type basis set[6] and Goedecker-Teter-Hutter (GTH) pseudopotentials[7, 8] combined with Gamma k-point and 400 eV cut-off energy. In the calculation steps, the energy minimization is used to balance the system, and then the Maxwell distribution method is used to give the molecules different collision probabilities, and then the dynamic process is carried out. The post processes analysis are performed by self-programs in Python.

The adsorption energy is calculated by the formula of:

$$E = E_{ads+sub} - E_{ads} - E_{sub} + E_{free\ energy\ correction} \qquad \textbf{Equation S1}$$

The formation energy is calculated and satisfied by:

$$E = E_{bulk} - E_{atomic} - \sum n_i \mu_i \qquad \textbf{Equation S2}$$

We aim at 2D perovskite, the initial state is 3D perovskite, and by sampling the formation of 2D perovskite, which is the formation energy of the intercalation process of organic matter, doing the reformation on the lattice scale.

Figure caption

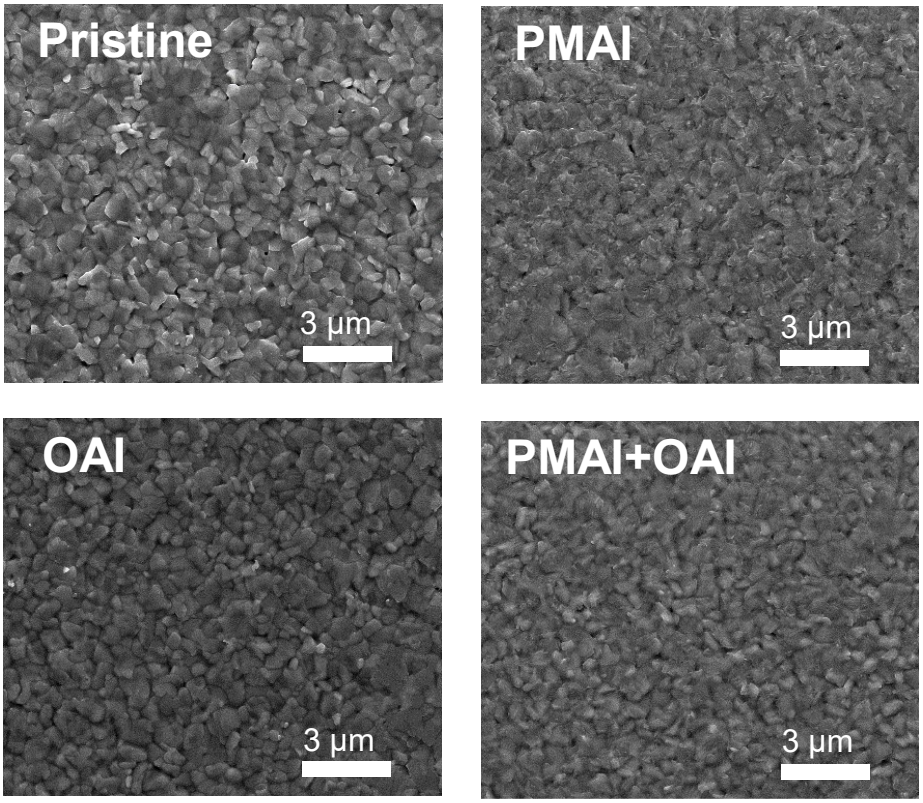

Figure S1. Top view SEM images of pristine, PMAI-treatment, OAI-treatment and OAI+PMAI treatment.

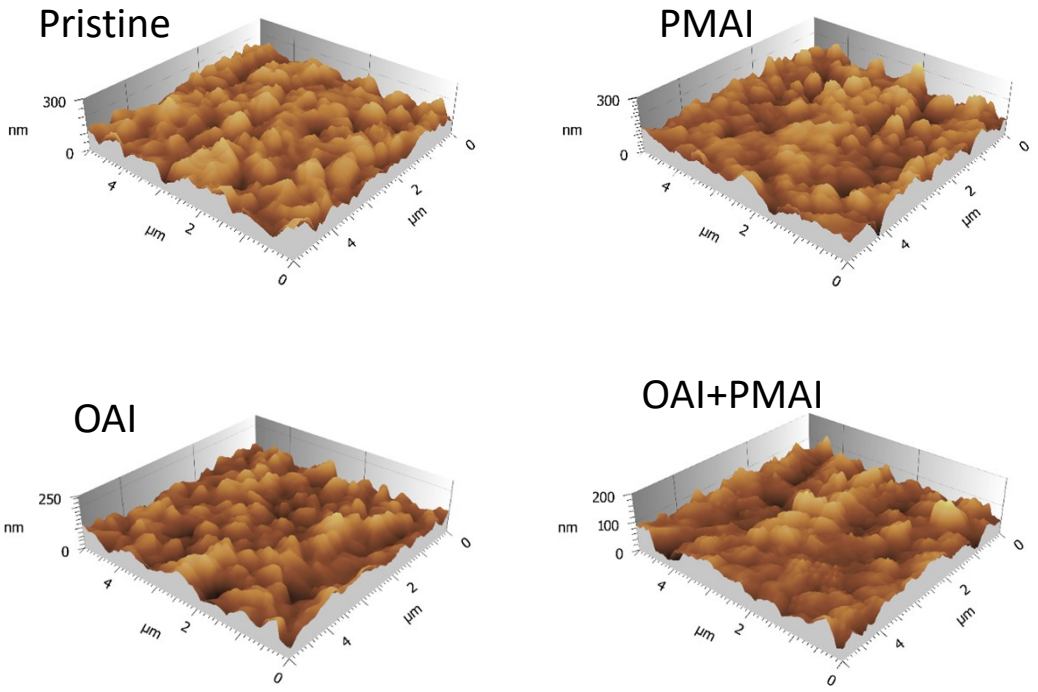

Figure S2. The 3D AFM images of pristine, PMAI-treatment, OAI-treatment and OAI+PMAI treatment.

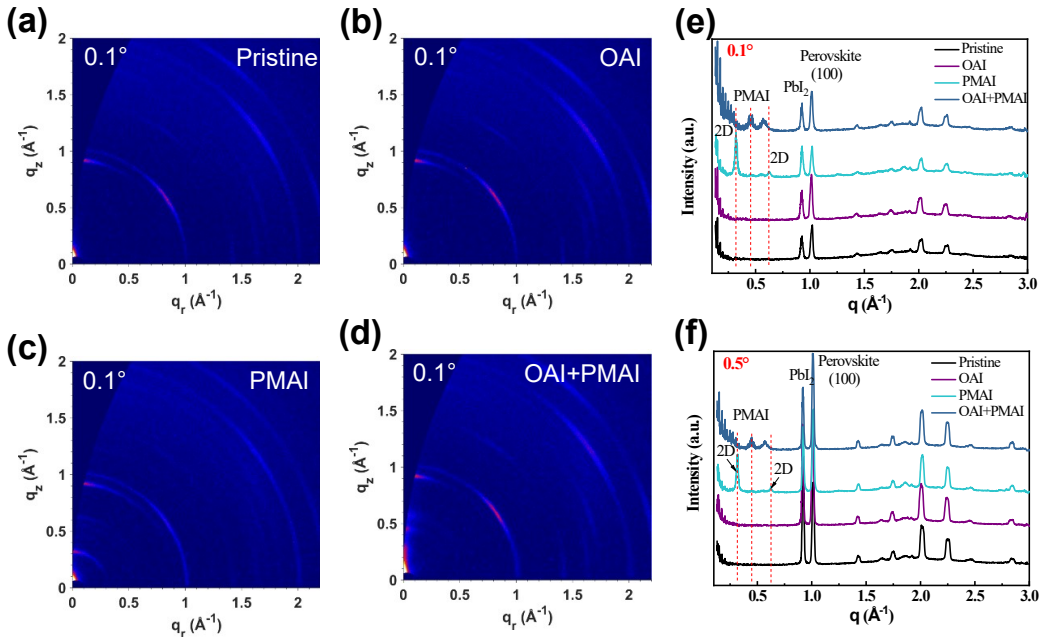

Figure S3. (a-d) GIWAXS mapping of different surface passivation treatments at a swept incidence angle of 0.1°. (e) GIWAXS intensity profiles for different surface passivation treatments at a swept incidence angle of 0.1°. (f) GIWAXS intensity profiles for different surface passivation treatments at a swept incidence angle of 0.5°.

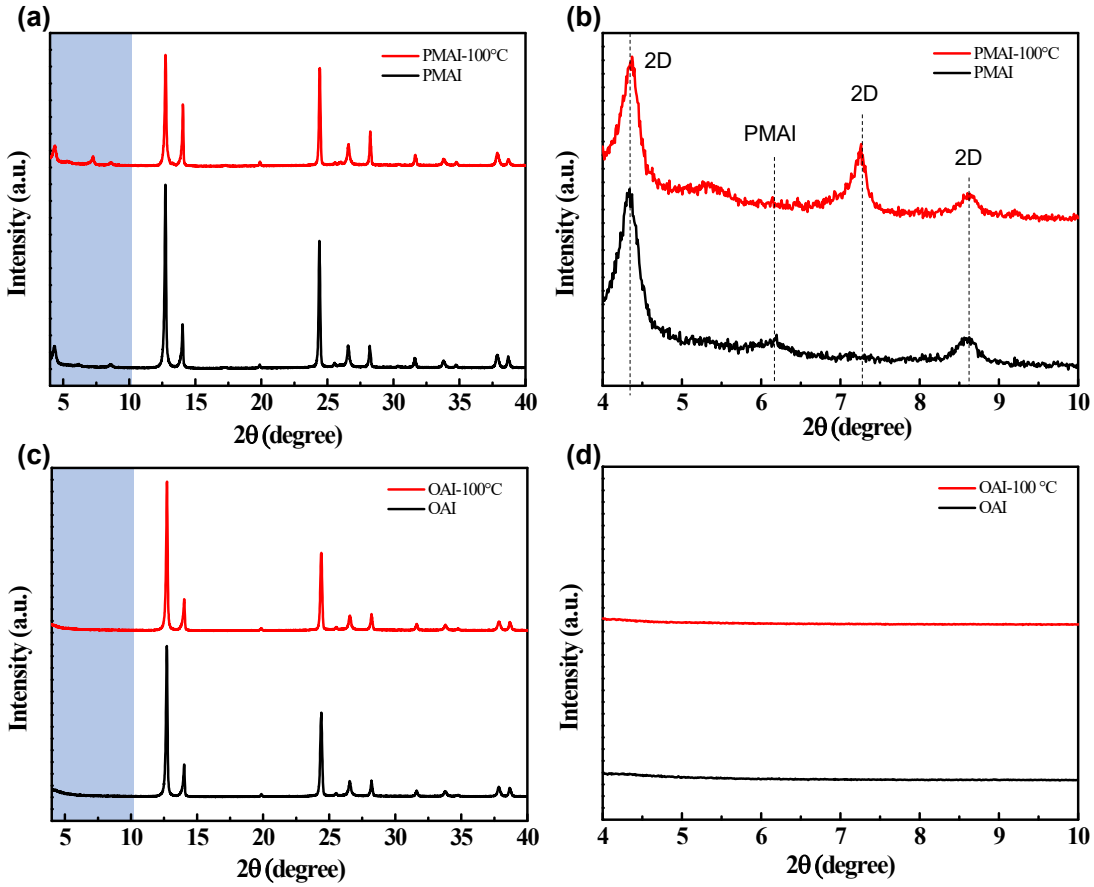

Figure. S4 XRD patterns of surface passivation without annealing treatment and annealing treatment by heating at 100 ℃ for 5 minutes. (a) PMAI passivation treatment and enlarged view of the shaded area (b). (C) OAI passivation treatment and enlarged view of the shaded area (d).

Note: After the PMAI spin coating passivation treatment, the PMAI on the film surface were almost completely converted to the 2D phase under heating. In contrast, no low-dimensional phase production were observed during the OAI treatment despite the annealing procedure.

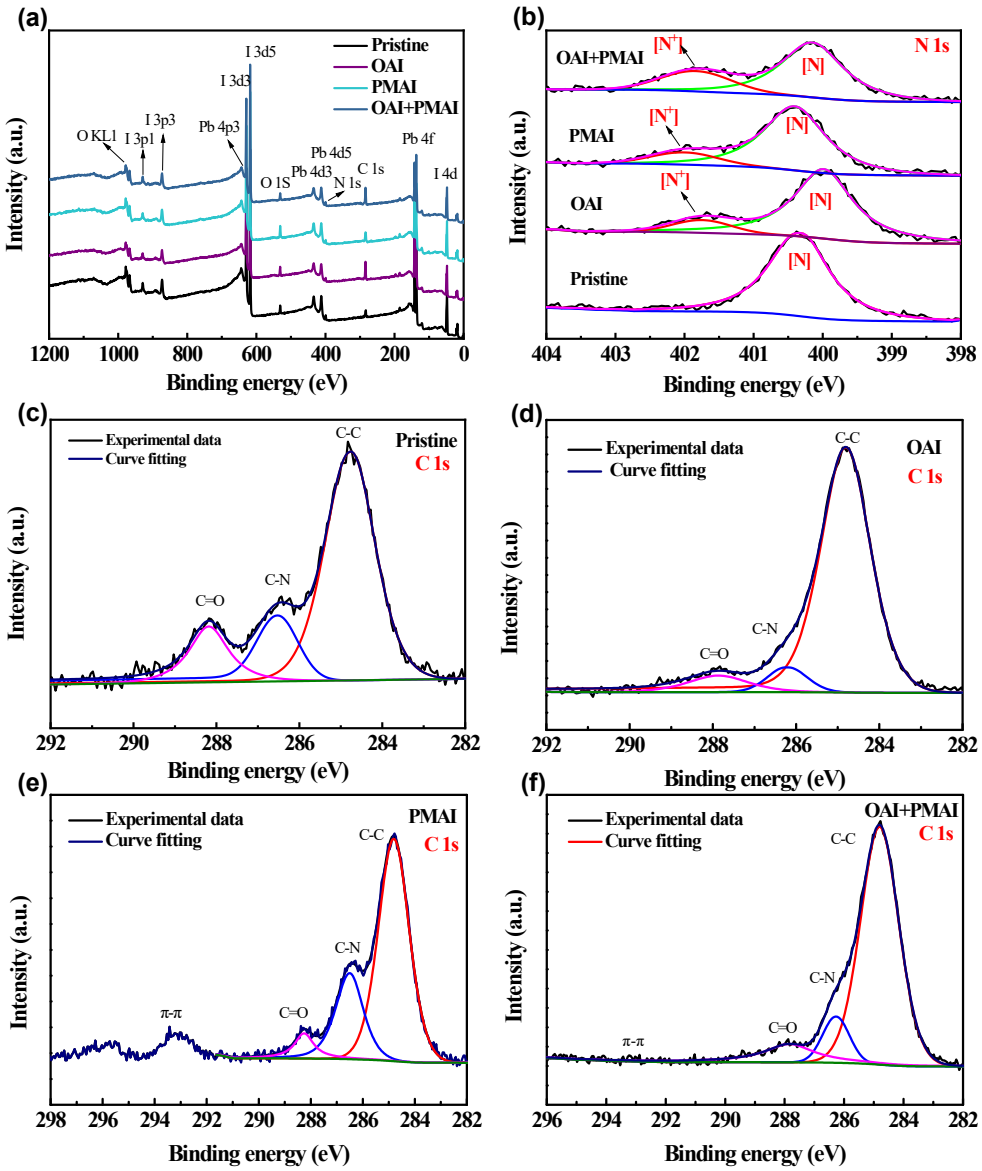

Figure S5. (a) Full XPS spectra of the perovskite films treatment in the range of 0 to 1200 eV binding energy. (b) XPS spectra of N1s. C 1s core level XPS spectra of different surface passivation schemes, (c) pristine, (d) OAI-treatment, (e) PMAI-treatment and (f) OAI+PMAI-treatment.

Compared to the pristine, additional peaks appeared in the N 1s core-electron spectra after various surface treatments, which confirmed the presence of surface ammonium salts (**Figure S5B**). The C 1s core-electron spectra are shown in **Figures S5C-S5F**, where the C-C and C-N bonds correspond to the presence of FA/MA cations. The peak with binding energy at around 293 eV corresponds to the π-π bond in phenyl group of the PMA^+ cation. Notably, we found that the C=O peak associated with oxygen/water (288.0 eV) was significantly suppressed after various surface treatments, especially minimized when OAI+PMAI co-treatment was used. (**Table S1**), which is beneficial for improving the long-term stability of the device[9].

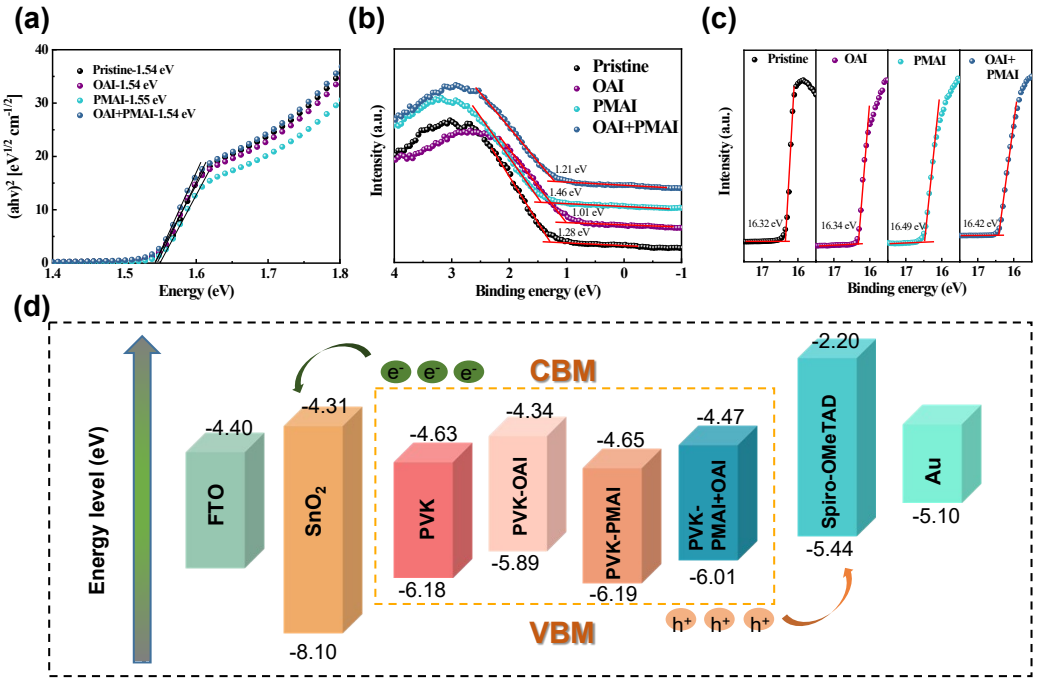

Figure S6. (a) Tauc plots for calculating optical band gaps from UV-vis absorption spectra. The UPS of perovskite film, the cut-off region (b) and the VBM (c) region. (d) Schematic energy level diagrams of perovskite solar cells.

Note: We investigated the change in energy levels of perovskite film surfaces before and after ammonium modulation using ultraviolet photoelectron spectroscopy (UPS) (Figures S6b and S6c). Compared with the pristine films, Fermi levels (Ef) of the films all shifted upward after ligand modulation, indicating that the self-doping effect of the perovskite films was alleviated[10]. A significant upward shift of valence band maximum (VBM) and conduction band minimum (CBM) were observed after OAI coating, shortening the energy barrier with the adjacent HTL. In contrast, energy band of the PMAI-coated perovskite film does not shift obviously, with the film surface shifted to a relatively intrinsic nature. Importantly, we found the shift of the energy levels lies between the cases treated coatings individually after the OAI+PMAI bi-molecular treatment. This optimized forbidden band is more favorable for smoothing the band alignments of the HTL and perovskite layers (Figure S6d). The reason is that the value of the energy level difference between adjacent layers is too narrow to facilitate the thermodynamic transfer of carriers. If the value is too different again, it will lead to V_{OC} loss.

OAI mainly provides the ability to shift the bandgap level up, while PMAI provides the positive dipole layer to further reduce the recombination loss.

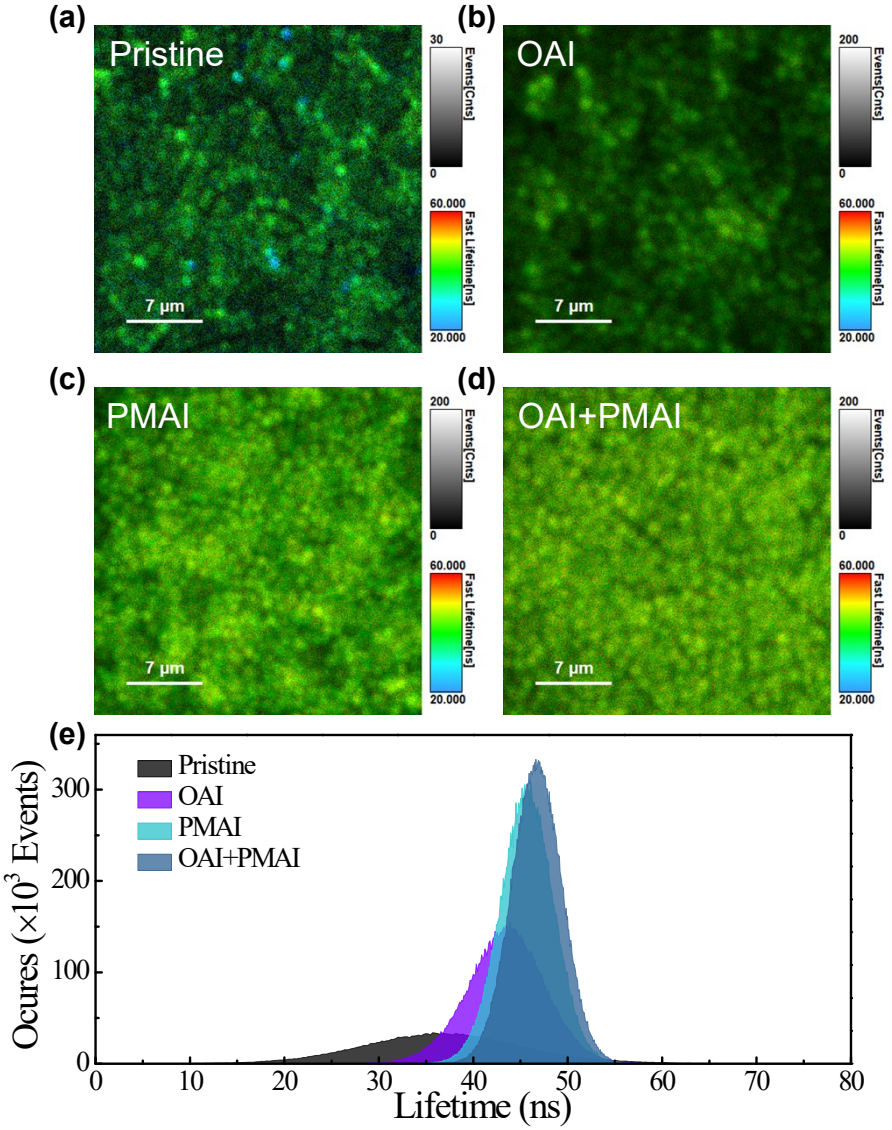

Figure S7. Time-resolved confocal fluorescence microscopy images of the control (a), OAI (b), PMAI (c) and OAI+PMAI (d) treated perovskite films. (e) PL occurs distribution of different carrier lifetime for the corresponding films.

We conducted an analysis of the spatially resolved distribution of charge carrier lifetime and photoluminescence (PL) intensity in perovskite thin films using TCFM. PL intensity maps and in-situ spatially resolved PL lifetime maps were displayed in the same image using grayscale and color scales, as shown in Figures S7 a-d. Due to spatial variations of trap-state distribution, all films exhibited pronounced spatial heterogeneity in PL intensity. In contrast, regions of short lifetime in the original film, depicted in light blue, transformed into areas of longer lifetime in light green and yellow-green after individual treatments with OAI and PMAI. Interestingly, after bi-molecular treatment with OAI+PMAI, the film exhibited even more yellow-green regions, indicating a significant prolongation of charge carrier lifetime. Both PL intensity and carrier lifetime across the gain region exceeded those at the grain boundaries, suggesting that defects are primarily located at the grain boundaries. It is noteworthy that the extraction of carrier lifetime distribution from TCFM images (Figure S7e) confirmed a substantial reduction of the light-blue regions in the OAI+PMAI bi-molecular treated film due to the increased average lifetime, consistent with the higher

crystallization quality and lower trap-state density of the film. These findings are in accordance with the above discussed PL and TPRL spectroscopic results.

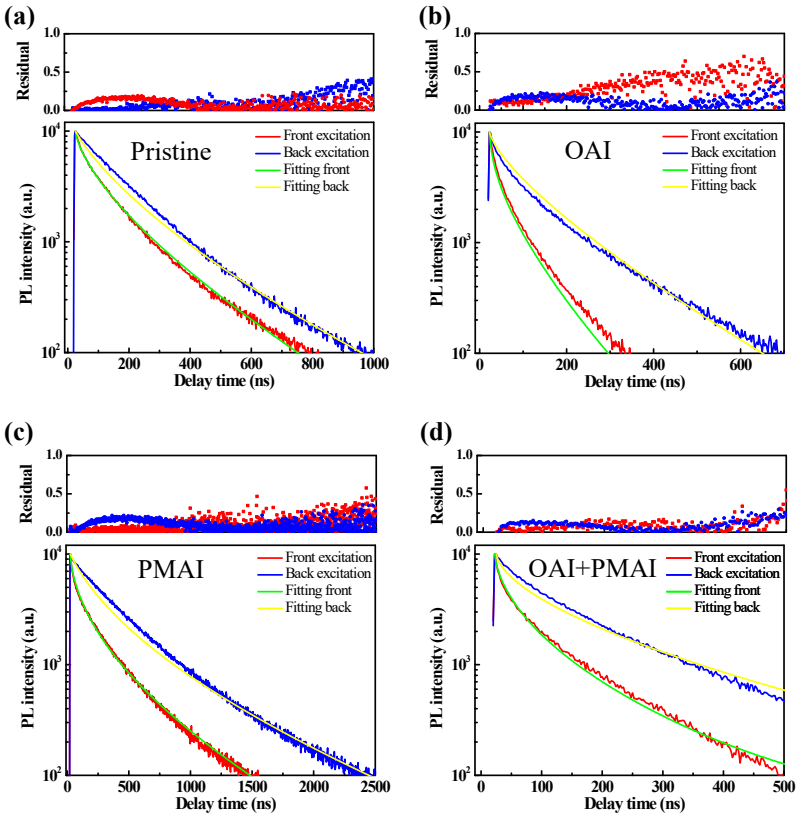

Figure S8. Fitting the TRPL measurements based on different surface passivation. The red and blue lines represent the experimental curves for frontal incidence and back incidence, respectively. The green and yellow lines correspond to the fitted curves, respectively.

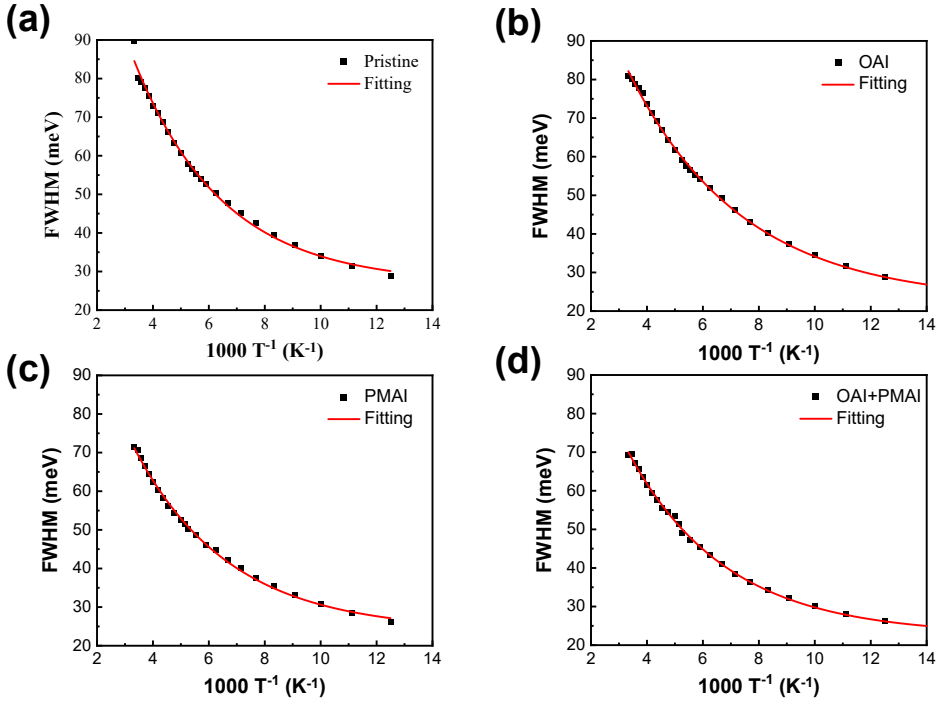

Figure S9. The temperature dependent PL measurements of the different surface treatment conditions. Temperature dependence of PL emission spectral width (FWHM) for different surface treated films in the range of 70 K to 300 K, (a) pristine, (b) OAI-treatment, c) PMAI-treatment and (d) OAI/PMAI-treatment.

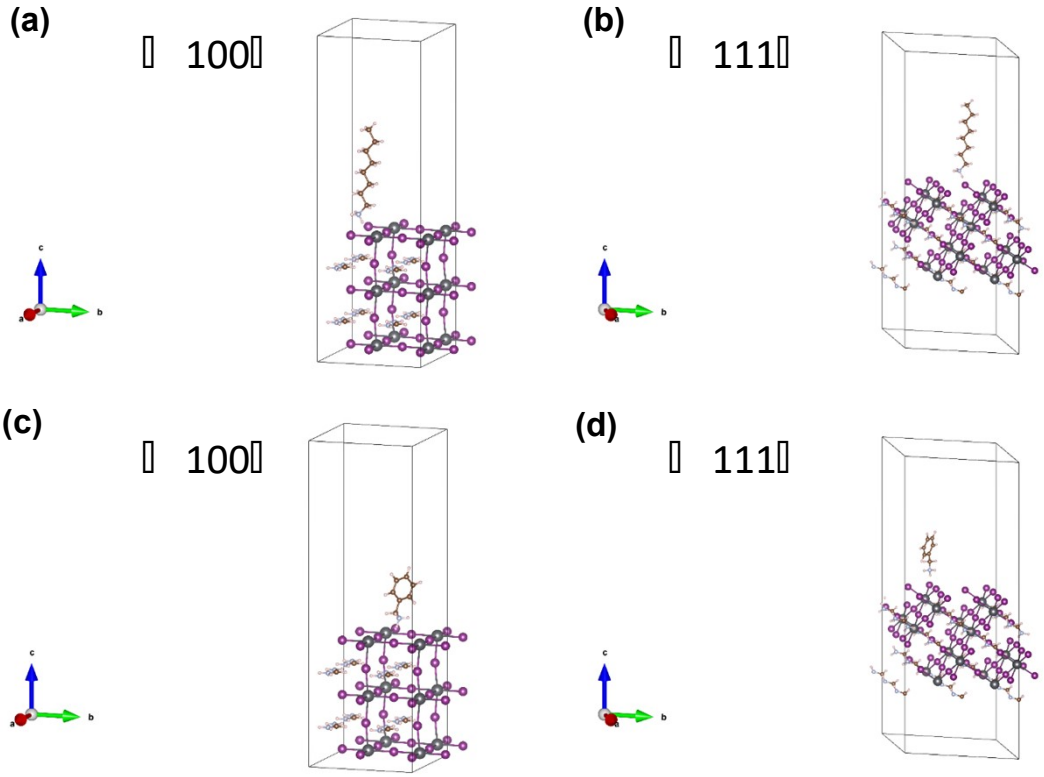

Figure S10. (a-d) Optimized structures for the adsorption of OA^+ and PMA^+ cation on the perovskite surface.

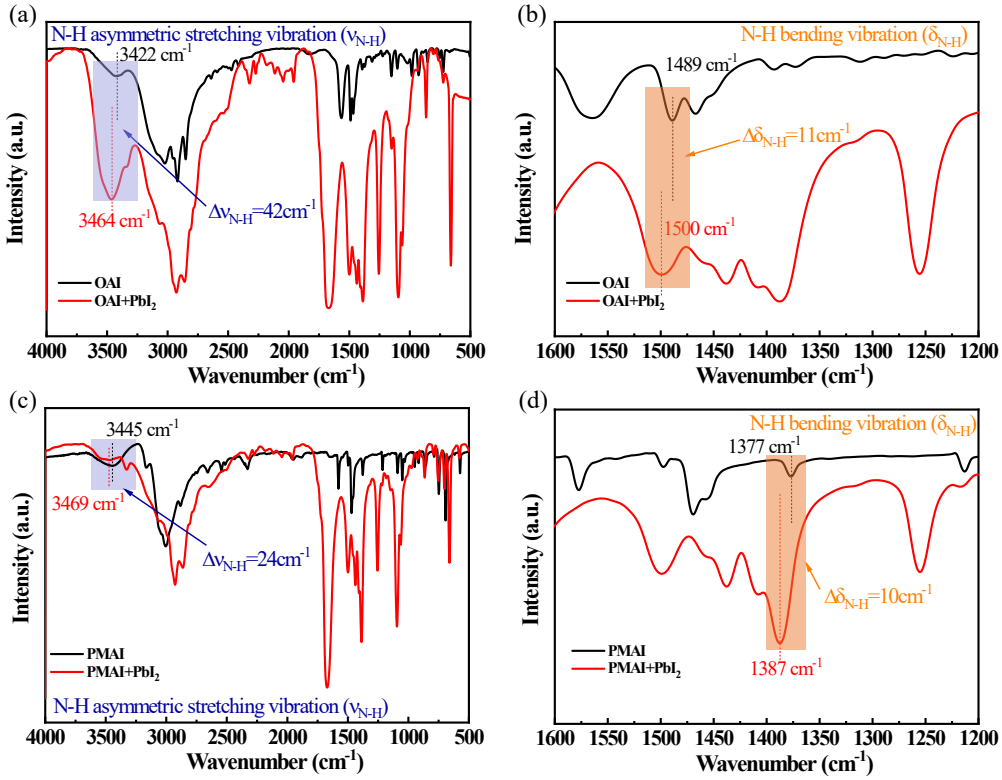

Figure S11. FTIR spectra of PbI_2 with and without OAI (a, b), with and without PMAI (c, d).

Note: The surface passivation effect is believed to stem from the interaction between the ammonium cation and the Pb-I framework. Changes in the N-H asymmetric stretching vibration (ν_{N-H}) and N-H bending vibration (δ_{N-H}) in the FTIR spectra can be observed upon the mixture of OAI and PMAI with PbI_2, respectively. It is noteworthy that the ν_{N-H} peak shifts from 3422 to 3464 cm^{-1}, and δ_{N-H} shifts from 1489 to 1500 cm^{-1} after the addition of PbI_2 to OAI. On the other hand, after the addition of PbI2 to PMAI, N-H peak shifts from 3445 to 3469 cm^{-1}, and δ_{N-H} shifts from 1377 to 1387 cm^{-1}. This suggests that OAI is very likely to exhibit a greater absorptivity on the perovskite film".

It is generally expected that the infrared vibrational peak of the N-H bond linking the H atom to the I atom through hydrogen bonding would move to a lower wave number position. However, this was not observed in our measurements. This is due to the dominant influence of the other three N-H bonds that are not involved in hydrogen bonding on the infrared properties of N-H in the hybrid system[11].

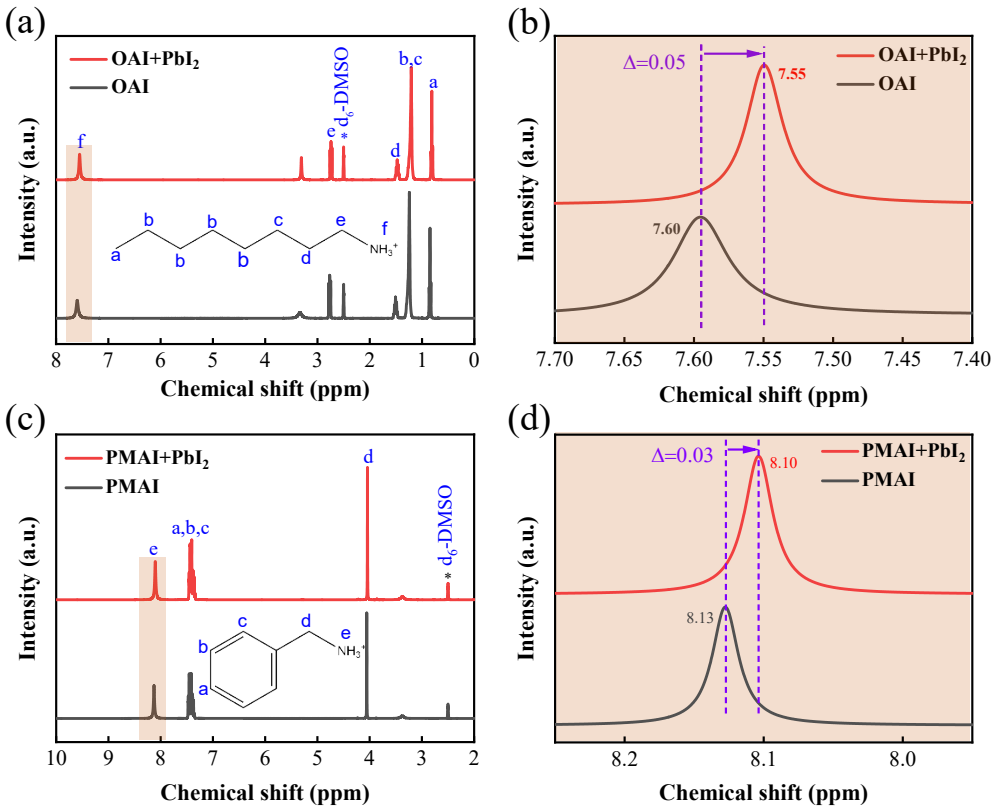

Figure S12. ^{1}H NMR spectra of (a, b) OAI, OAI+PbI_2, (c, d) PMAI and PMAI+ PbI_2.

In these NMR spectra, the two peak signals at 7.60 ppm and 8.13 ppm correspond to the NH_3 proton peaks of OAI and PMAI, respectively. Clearly, the significant shift of the proton peak for OAI, when the passivators are mixed with PbI_2 separately, implies a stronger NH···I hydrogen bonding interaction with the inorganic $[PbI_6]^{4-}$ octahedral layer.

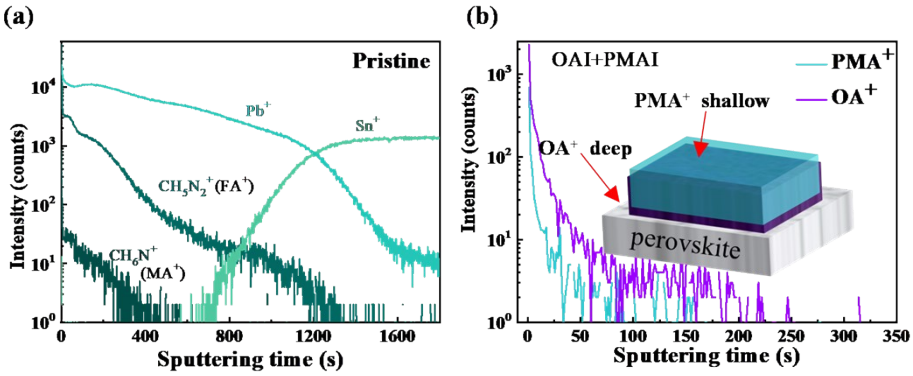

Figure S13. ToF-SIMS depth profiles of the pristine (a). (b) Enlarged view of OAI+PMAI treatment, inset illustrates the spatial distribution of both.

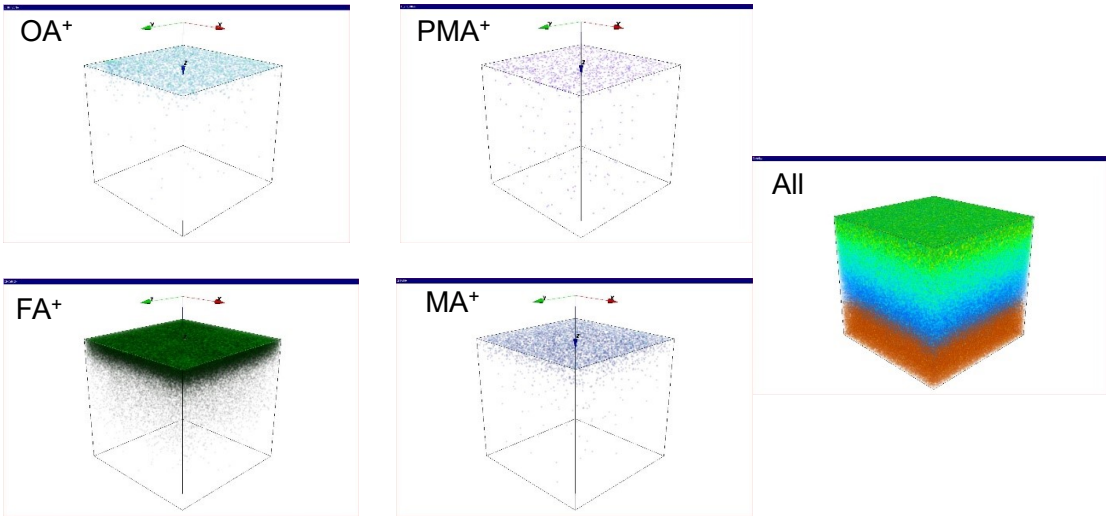

Figure S14. Three-dimensional reconstructed images of OAI/PMAI bi-molecular passivation-treated perovskite films. The tracked ions are all positively charged monovalent fragments and the tracked m/z values are 45 ($CH(NH_2)_2^+$) for FA, 32 ($CH_3NH_3^+$) for MA, 208 (Pb^+) for Pb,119 (Sn^{4+}) for Sn, 130 ($C_8H_{20}N^+$) for OA, 108 ($C_7H_{10}N^+$) for PMA.

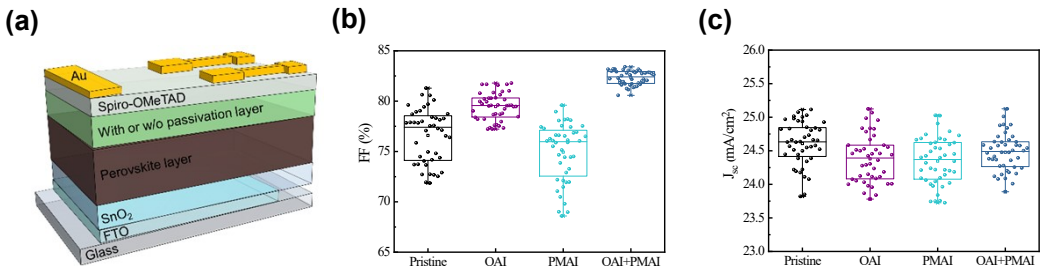

Figure S15. (a) The devices structure of perovskite solar cells. (b) and (c) Distribution of fill factor and short-circuit current density.

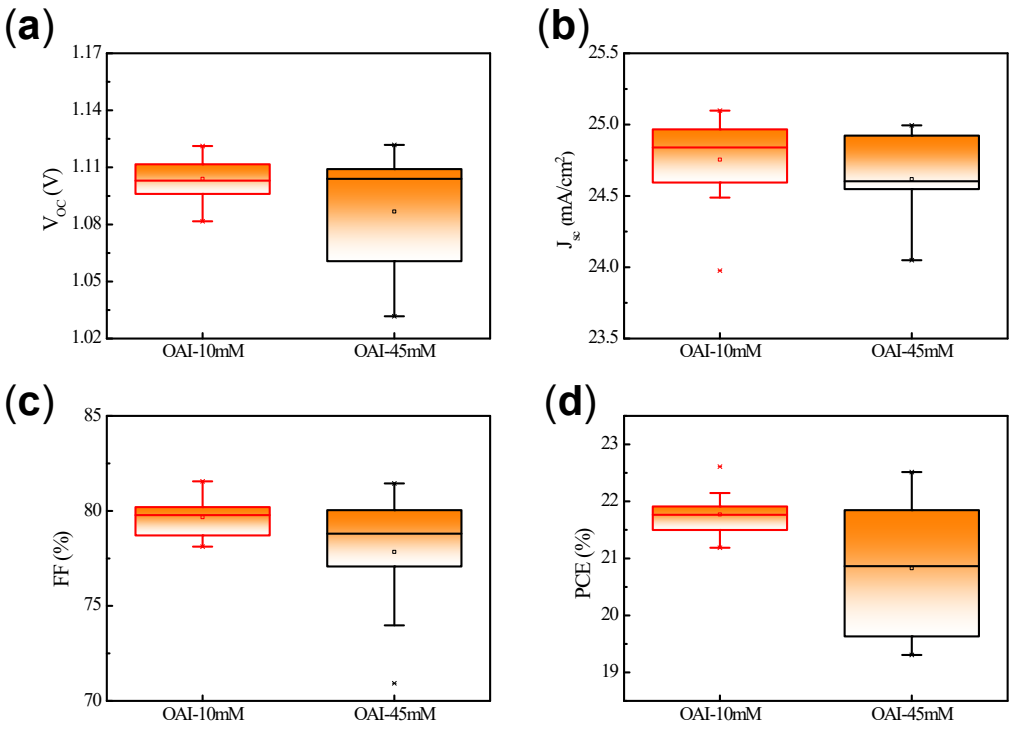

Figure S16. Statistical distribution of optoelectronic performance of surfaces treated with different OAI concentrations. (a) Open circuit voltage. (b) Short-circuit current. (c) Fill factor. (d) Power conversion.

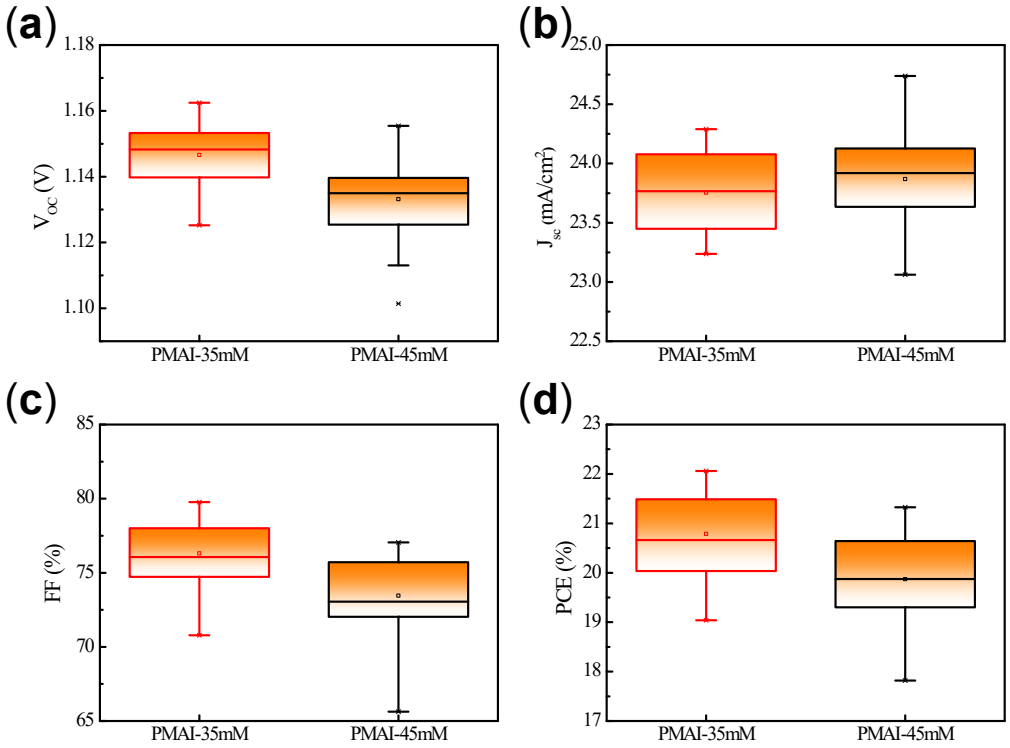

Figure S17. Statistical distribution of optoelectronic performanceof surfaces treated with different PMAI concentrations. (a) Open circuit voltage. (b) Short-circuit current. (c) Fill factor. (d) Power conversion.

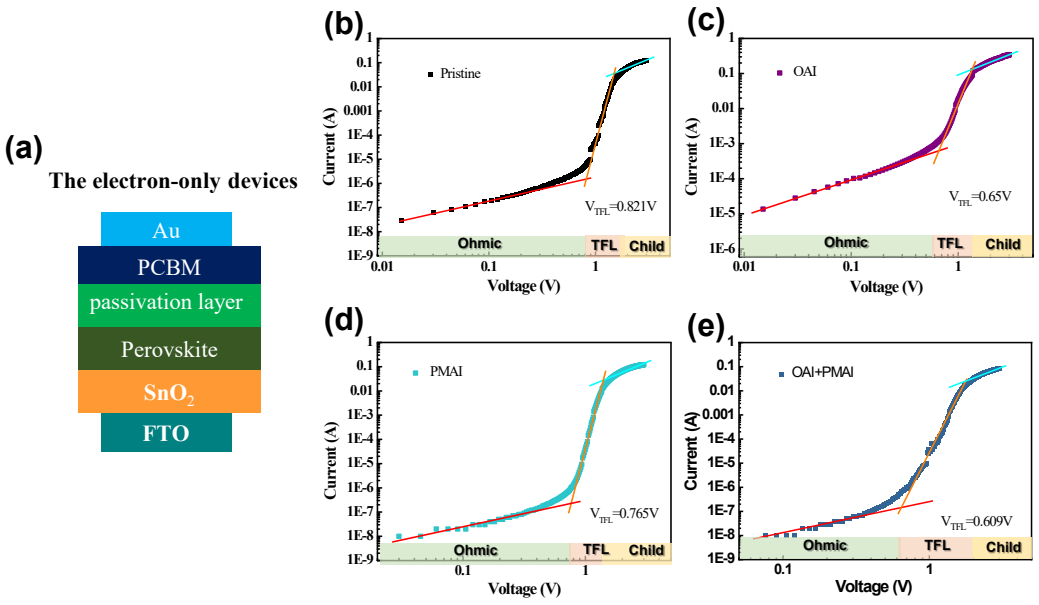

Figure S18. Space charge limited current (SCLC) measurements of defect density under different treatment conditions. (a) Schematic diagram of electron-only device

structure. C–V curves for electron-only devices with (b) pristine, (c) OAI-treatment, (d) PMAI-treatment and (e) OAI/PMAI-treatment.

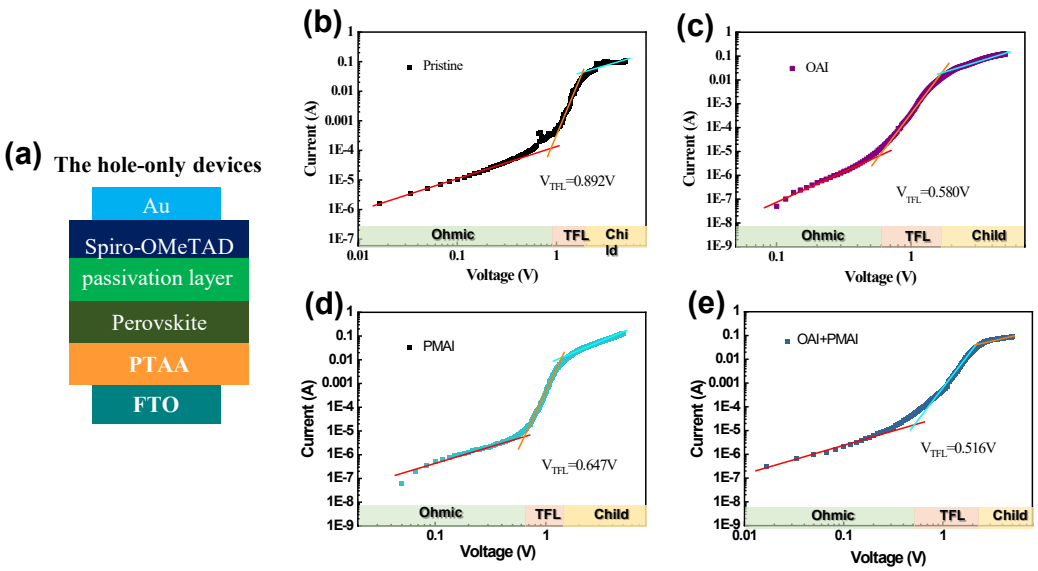

Figure S19. Space charge limited current (SCLC) measurements of defect density under different treatment conditions. (a) Schematic diagram of hole-only device structure. C–V curves for hole-only devices with (b) pristine, (c) OAI-treatment, (d) PMAI-treatment and (e) OAI/PMAI-treatment.

Note：The trap densities of different films were calculated by the space charge-limited current (SCLC) method. The dark currents of these devices are measured under an applied bias voltage, and the trap filling limit (TFL) region starts to increase abruptly when the bias voltage exceeds the twist junction. The trap fill limit voltage (V_{TFL}) is the applied voltage at the kink point, i.e. the starting voltage in the TFL region. The trap density of states is calculated using the following equation:

$$N_t = \frac{2\varepsilon_0\varepsilon_r V_{TFL}}{eL^2}$$

where ε_0 is the relative permittivity, N_t represents the trap density, ε_r is the vacuum tolerance, e is the fundamental charge, and L is the thickness of the perovskite film. The thickness of the film we set to 800 nm, which is the classical thickness of the perovskite film prepared by the two-step method.

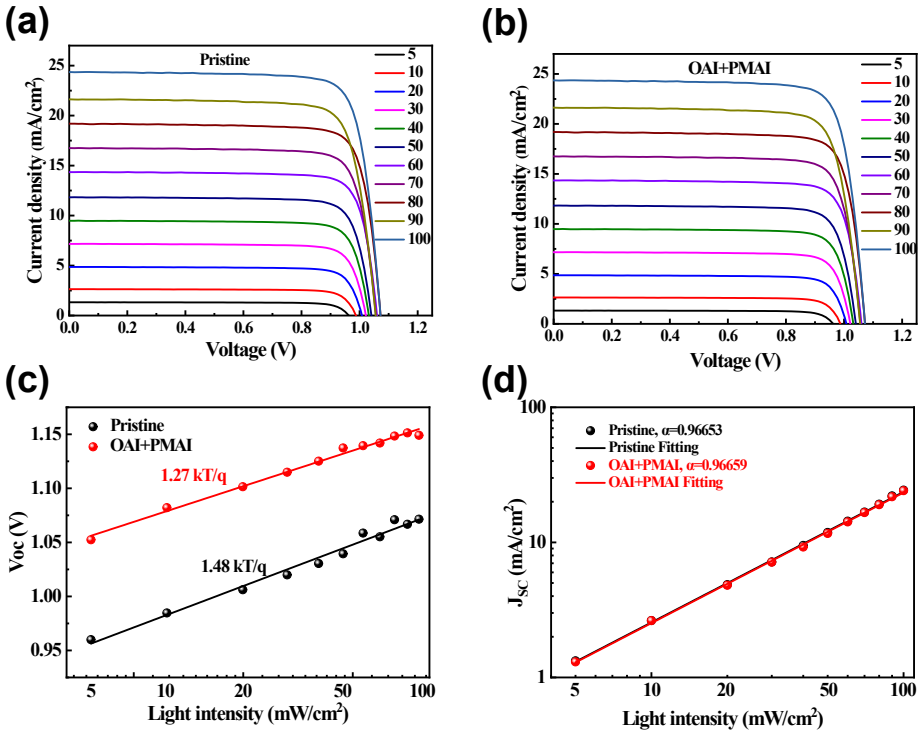

Figure S20. The response of devices under different light intensities for the pristine and OAI+PMAI (target) treated devices. (a) J-V curve of the pristine device and (b) OAI+PMAI bi-molecular treatment under different light intensity. Linear relationship of (c) V_{OC} and (d) J_{SC} with the natural logarithmic light intensity.

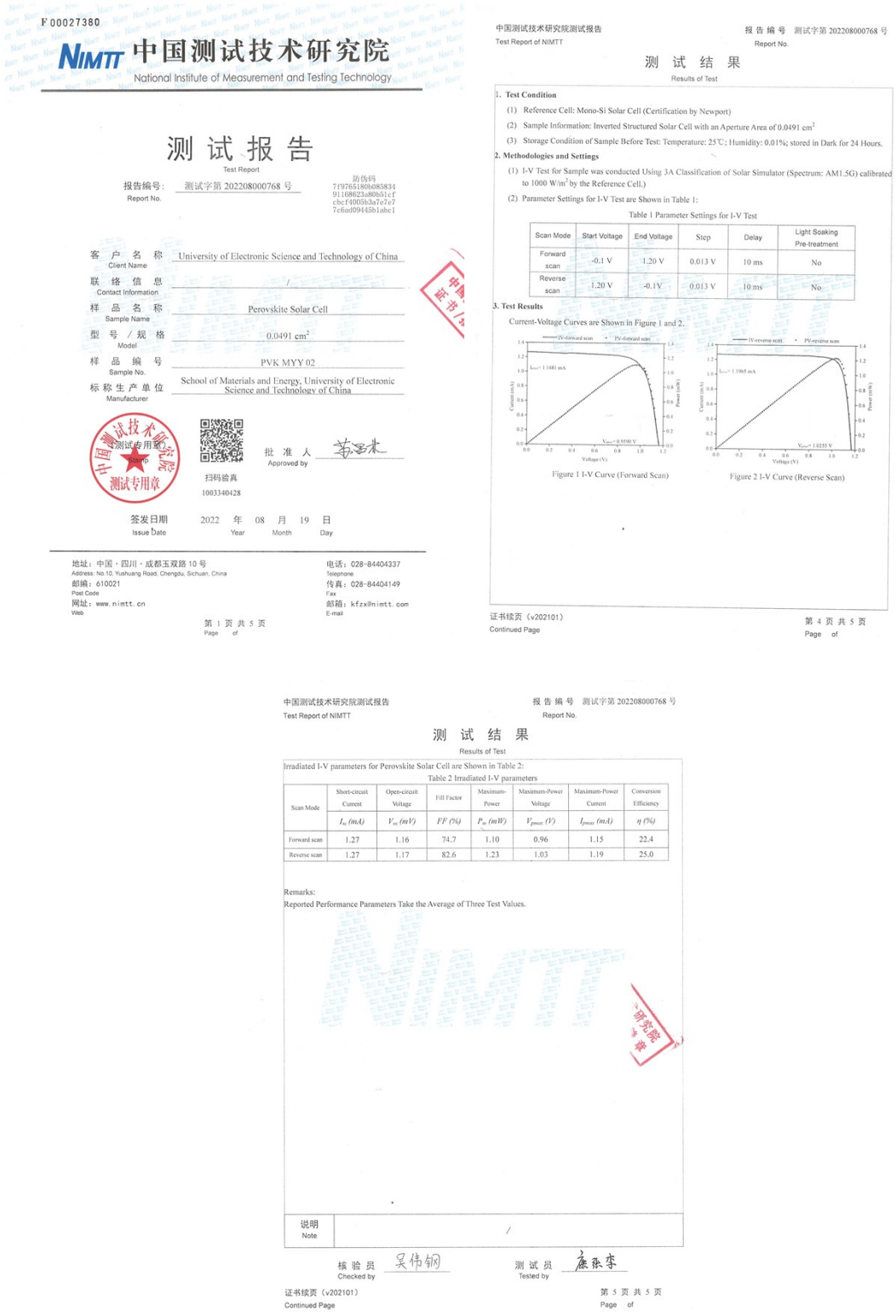

F 00027380

NIMTT 中国测试技术研究院
National Institute of Measurement and Testing Technology

测 试 报 告
Test Report

报告编号：测试字第 202208000768 号
Report No.

防伪码
7f9765180b085834
91168623a80b51cf
cbcf4005b3a7e7e7
7c6ad09445b1abc1

客 户 名 称 Client Name: University of Electronic Science and Technology of China
联 络 信 息 Contact Information: /
样 品 名 称 Sample Name: Perovskite Solar Cell
型 号 / 规 格 Model: 0.0491 cm^2
样 品 编 号 Sample No.: PVK MYY 02
标称生产单位 Manufacturer: School of Materials and Energy, University of Electronic Science and Technology of China

扫码验真
1003340428

批 准 人 Approved by
签发日期 Issue Date: 2022 年 Year 08 月 Month 19 日 Day

地址：中国·四川·成都玉双路 10 号
Address: No.10, Yushuang Road, Chengdu, Sichuan, China
邮编：610021
Post Code
网址：www.nimtt.cn
Web
电话：028-84404337
Telephone
传真：028-84404149
Fax
邮箱：kfzx@nimtt.com
E-mail

第 1 页 共 5 页
Page of

中国测试技术研究院测试报告
Test Report of NIMTT

报告编号 测试字第 202208000768 号
Report No.

测 试 结 果
Results of Test

1. Test Condition
(1) Reference Cell: Mono-Si Solar Cell (Certification by Newport)
(2) Sample Information: Inverted Structured Solar Cell with an Aperture Area of 0.0491 cm^2
(3) Storage Condition of Sample Before Test: Temperature: 25℃; Humidity: 0.01%; stored in Dark for 24 Hours.

2. Methodologies and Settings
(1) I-V Test for Sample was conducted Using 3A Classification of Solar Simulator (Spectrum: AM1.5G) calibrated to 1000 W/m^2 by the Reference Cell.)
(2) Parameter Settings for I-V Test are Shown in Table 1:

Table 1 Parameter Settings for I-V Test

Scan Mode	Start Voltage	End Voltage	Step	Delay	Light Soaking Pre-treatment
Forward scan	-0.1 V	1.20 V	0.013 V	10 ms	No
Reverse scan	1.20 V	-0.1V	0.013 V	10 ms	No

3. Test Results
Current-Voltage Curves are Shown in Figure 1 and 2.

Figure 1 I-V Curve (Forward Scan)

Figure 2 I-V Curve (Reverse Scan)

证书续页（v202101）
Continued Page

第 4 页 共 5 页
Page of

中国测试技术研究院测试报告
Test Report of NIMTT

报告编号 测试字第 202208000768 号
Report No.

测 试 结 果
Results of Test

Irradiated I-V parameters for Perovskite Solar Cell are Shown in Table 2:

Table 2 Irradiated I-V parameters

Scan Mode	Short-circuit Current	Open-circuit Voltage	Fill Factor	Maximum-Power	Maximum-Power Voltage	Maximum-Power Current	Conversion Efficiency
	I_{sc} (mA)	V_{oc} (mV)	FF (%)	P_m (mW)	V_{pmax} (V)	I_{pmax} (mA)	η (%)
Forward scan	1.27	1.16	74.7	1.10	0.96	1.15	22.4
Reverse scan	1.27	1.17	82.6	1.23	1.03	1.19	25.0

Remarks:
Reported Performance Parameters Take the Average of Three Test Values.

说明 Note	/

核验员 Checked by
测试员 Tested by

证书续页（v202101）
Continued Page

第 5 页 共 5 页
Page of

Figure S21. Test report from National Institute of Measurement and Testing Technology, Power conversion efficiency of 25.0% for single-junction perovskite solar cells implementing OAI/PMAI bi-molecular passivation strategy on the surface of perovskite films.

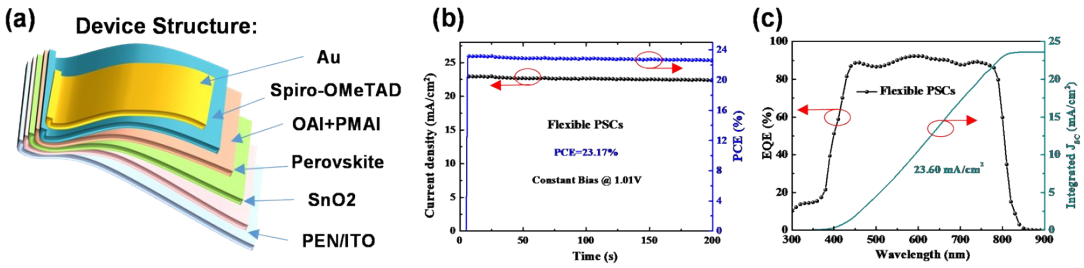

Figure S22. (a) The structure diagram of flexible PSCs. (b) The stable output of champion flexible device at V_{bis}=1.01 V. (c) EQE spectrum and the corresponding integrated current density of the champion flexible device after the addition of the reflective reduction layer.

Table S1. Fitting results of C1s core energy levels for different surface treatment cases

Samples	C=O	C-N	C-C	Area ratio
Pristine	0.24	0.27	1	0.24
OAI	0.07	0.1	1	0.07
PMAI	0.1	0.37	1	0.1
OAI+PMAI	0.08	0.19	1	0.08

Table S2. Summary the TRPL of the perovskite films fitted by bi-exponential decay function: $y = A_1\exp(-t/\tau_1) + A_2\exp(-t/\tau_2) + B$. The average lifetime ($\tau_{ave}$) is obtained via the relation $\tau_{ave} = (A_1\tau_1^2 + A_2\tau_2^2)/(A1\tau1 + A_2\tau_2)$. Where A_1 and A_2 are the decay amplitudes, and τ_1 and τ_2 are the decay time constants.

Samples	A_1	τ_1 (μs)	A_2	τ_2 (μs)	τ_{av} (μs)
pristine	5360.7	0.381	3236.0	0.055	0.355
OAI	1781.7	0.691	3269.0	0.168	0.529
PMAI	3629.0	0.786	4054.7	0.249	0.646
OAI+PMAI	4260.3	1.056	2397.0	0.060	1.026

Table S3. List of best fitting results of charge carrier dynamics parameters.

	Pristine	OAI	PMAI	OAI+PMAI
D[m^2/s]	4.55×10^{-9}	1.76×10^{-8}	4.5×10^{-9}	6.99×10-9
k_1[s^{-1}]	1.565×10^{6}	4.425×10^{6}	5×10^{5}	2×10^{6}
k_2[cm^3/s]	8×10^{-10}	7.6×10^{-11}	6.77×10^{-10}	1.07×10^{-10}
S_0[m/s]	5.06	2.65	8.19	0.8
S_L[m/s]	0.08	0.09	0.06	0.05

Table S4. The Boson model fitting parameters from the FWHM vs. temperature plots.

Samples	Γ_0 (m eV)	Γ_{op} (m eV)	E_{op} (m eV)	R^2
Pristine	26.92±1.34	60.58±2.93	0.027±0.00152	0.998
OAI	22.52±0.61	49.72±0.71	0.021±0.00049	0.998
PMAI	23.89±0.65	46.07±1.05	0.025±0.00083	0.998
OAI+PMAI	22.70±0.49	45.03±0.93	0.024±0.00064	0.998

Table S5. Summary of fitting impedance spectroscopy.

Samples	R_S (Ω)	R_C (Ω)	CPE
Pristine	12.7	240.6	2.09×10^{-8}
OAI	13.3	183	1.48×10^{-8}
PMAI	4.95	277	7.2×10^{-8}
OAI+PMAI	15.6	80.8	5.79×10^{-8}

Table S6. Space-limited charge current (SCLC) calculation results of the electron-only devices based on the Pristine, OAI, PMAI and OAI+PMAI PSCs, respectively. The thickness of perovskite film is estimated at 800 nm.

Samples	V_{TFL} (v)	N_{trap} (cm^{-3})
Pristine	0.821	$8.83*10^{15}$
OAI	0.659	$7.09*10^{15}$
PMAI	0.765	$8.23*10^{15}$
OAI+PMAI	0.609	$6.55*10^{15}$

Table S7. Space-limited charge current (SCLC) calculation results of the hole-only devices based on the Pristine, OAI, PMAI and OAI+PMAI PSCs, respectively. The thickness of perovskite film is estimated at 800 nm.

Samples	V_{TFL} (v)	N_{trap} (cm^{-3})
Pristine	0.892	$9.59*10^{15}$
OAI	0.580	$6.24*10^{15}$
PMAI	0.647	$6.96*10^{15}$
OAI+PMAI	0.516	$5.55*10^{15}$

Table S8. The photovoltaic performance parameters of 50 randomly optimized device samples treated with OAI+PMAI bi-molecular passivation.

Sample	V_{OC} (V)	J_{SC} (mA/cm²)	Fill Factor（%）	Efficiency（%）
1#	1.159	25.092	82.934	24.118
2#	1.163	25.427	83.167	24.589
3#	1.161	25.206	83.513	24.450
4#	1.161	24.806	84.017	24.195
5#	1.160	25.056	83.840	24.371
6#	1.163	25.637	84.391	25.153
7#	1.163	25.120	84.232	24.602
8#	1.161	25.756	84.349	25.230
9#	1.160	25.504	82.788	24.502
10#	1.162	24.988	84.204	24.459
11#	1.163	25.459	84.045	24.878
12#	1.162	25.098	84.697	24.698
13#	1.158	25.272	83.006	24.289
14#	1.163	25.136	84.446	24.691
15#	1.161	24.923	83.822	24.259
16#	1.162	24.918	84.863	24.566
17#	1.160	24.914	83.168	24.030
18#	1.162	25.450	85.034	25.142
19#	1.163	25.168	84.116	24.626
20#	1.164	25.269	82.916	24.387
21#	1.163	25.624	83.605	24.910
22#	1.169	25.160	84.261	24.783
23#	1.165	25.160	84.516	24.765
24#	1.160	25.625	83.356	24.782
25#	1.164	25.217	84.628	24.845
26#	1.168	25.543	81.545	24.331
27#	1.167	26.015	80.140	24.327

28#	1.169	25.327	81.954	24.265
29#	1.158	25.529	81.263	24.020
30#	1.169	25.885	82.613	24.991
31#	1.173	25.212	83.458	24.674
32#	1.174	25.436	82.902	24.748
33#	1.166	25.508	81.117	24.129
34#	1.170	25.121	82.440	24.230
35#	1.170	25.282	81.764	24.193
36#	1.171	25.434	82.489	24.573
37#	1.173	25.386	82.161	24.469
38#	1.176	24.951	83.068	24.367
39#	1.172	25.817	81.406	24.630
40#	1.175	25.254	82.341	24.425
41#	1.168	24.989	82.377	24.045
42#	1.168	25.491	81.926	24.394
43#	1.169	25.879	81.619	24.692
44#	1.169	25.946	81.664	24.777
45#	1.173	25.671	82.916	24.967
46#	1.168	25.959	79.950	24.251
47#	1.171	25.618	82.134	24.637
48#	1.174	25.790	82.316	24.930
49#	1.174	25.938	82.103	24.998
50#	1.173	25.491	81.783	24.452
Average	**1.166**	**25.389**	**82.947**	**24.556**

Table S9. PCEs versus time for unencapsulated devices stored in ambient condition

Condition	Time (h)	PCE (%)	Retention rate (%)	Deviation (%)
Pristine	0	19.59817	100	0.36902
	73	18.67255	95.27	0.52534
	490	18.10685	92.39	0.84835
	976	18.09482	92.32	1.36787
	1440	19.06632	97.28	0.86259
OAI	0	20.88634	100	0.55881
	73	19.65161	94.08	0.50782
	490	18.83957	90.20	1.19885
	976	18.51158	88.63	0.79087
	1440	18.98991	90.92	0.72763
PMAI	0	21.45849	100	0.93711
	73	20.30379	94.61	0.77768
	490	13.71424	63.91	2.54626
	976	14.6306	68.18	1.67939

	1440	13.99036	65.19	1.63558
OAI+PMAI	0	21.95681	100	0.95956
	73	22.06948	105.51	0.7623
	490	21.59597	98.35	0.84762
	976	20.67001	94.14	1.35544
	1440	21.65987	98.64	0.35272

Table S10. Summary on representative progress of state-of-the-art perovskite solar cells by two-step fabrication under n-i-p configuration since 2019.

Years	V_{OC} (V)	J_{SC} (mA cm^{-2})	FF (%)	PCE (%)	Type of cations	References
2019	1.16	24.9	81.4	23.56	Mixed-cations (FAMA)	Nature Photonics, 2019, 13(7): 460-466.
2020	1.16	24.8	81.3	23.5	Mixed-cations (FAMAGA)	Advanced Materials. 2020, 32, 11.
2021	1.18	24.95	81.58	24.01	Mixed-cations (FAMA)	Energy Environ. Sci., 2021,14, 5074-5083
2021	1.17	25.34	81.36	24.1	Single -cations (FA)	Science,2021, 371, 1359
2021	1.16	25.01	83.44	24.27	Mixed-cations (FAMACs)	Science, 2021, 373(6554): 561-567
2022	1.18	25.0	82.7	24.4	Mixed-cations (FAMA)	Advanced Materials, 2022, 34(8): 2106118.
2022	1.17	25.30	84.2	24.95	Mixed-cations (FAMA)	Joule, 2022, 6(12): 2869-2884.
2022	1.18	26.3	82.7	25.6	Single -cations (FA)	Science,2022,377, 531–534
2023	1.171	25.28	84.57	25.03	Mixed-cations (FAMA)	Advanced Materials, 2023: 2210186.
2023	1.18	25.77	83.50	25.39	Single-cations (FA)	Nature Communications, 2023, 14(1): 6125.
2023	1.17	25.72	83.67	25.17	Mixed-cations (FAMA)	Nature Photonics, 2023: 1-9
2023	1.19	26.39	82.94	26.07	Single-cations (FA)	Nature, (2023) 1476-4687 (online)
2023	**1.16**	**25.76**	**84.35**	**25.23**	**Mixed-cations (FAMA)**	**This work**

References

1. K.-i. Ataka, T. Yotsuyanagi and M. Osawa, *J Phys Chem C*, 1996, **100**, 10664-10672.
2. H. A. Posch, W. G. Hoover and F. J. Vesely, *Physical Review A*, 1986, **33**, 4253-4265.
3. W. G. Hoover and B. L. Holian, *Physics Letters A*, 1996, **211**, 253-257.
4. W. Kohn and L. J. Sham, *Physical Review*, 1965, **140**, A1133-A1138.
5. T. Yanai, D. P. Tew and N. C. Handy, *Chemical Physics Letters*, 2004, **393**, 51-57.
6. J. F. Li, Y. F. Huang, Y. Ding, Z. L. Yang, S. B. Li, X. S. Zhou, F. R. Fan, W. Zhang, Z. Y. Zhou, D. Y. Wu, B. Ren, Z. L. Wang and Z. Q. Tian, *Nature*, 2010, **464**, 392-395.
7. Z. D. Schultz, S. K. Shaw and A. A. Gewirth, *Journal of the American Chemical Society*, 2005, **127**, 15916-15922.
8. W.-T. Liu and Y. R. Shen, *Proc. Natl. Acad. Sci. U. S. A.*, 2014, **111**, 1293-1297.
9. Q. Jiang, Y. Zhao, X. Zhang, X. Yang, Y. Chen, Z. Chu, Q. Ye, X. Li, Z. Yin and J. You, *Nat. Photonics*, 2019, **13**, 460-466.
10. D. Meggiolaro, D. Ricciarelli, A. A. Alasmari, F. A. S. Alasmary and F. De Angelis, *J. Phys. Chem. Lett.*, 2020, **11**, 3546-3556.
11. S. Tan, J. Shi, B. Yu, W. Zhao, Y. Li, Y. Li, H. Wu, Y. Luo, D. Li and Q. Meng, *Adv. Funct. Mater.*, 2021, **31**, 2010813.